

Strain Rate-Dependent Anomalous Work Hardening of a Single-Crystalline CoNi-Base Superalloy



J. VOLLHÜTER, A. BEZOLD, N. KARPSTEIN, M. KÖBRICH, E. SPIECKER, M. GÖKEN, and S. NEUMEIER

The deformation mechanisms operating in superalloys depend on different parameters such as composition, temperature and deformation rate. So far, the transition from shearing by APB-coupled dislocations to shearing under the formation of stacking faults has been studied exclusively as a function of temperature but not as a function of the strain rate. Therefore, interrupted compression tests with strain rates between 10^{-3} s^{-1} and 10^{-5} s^{-1} were performed on the single-crystalline CoNi-base superalloy ERBOCo-4 at a temperature of 850 °C. The evolution of the defect structures has been analyzed by conventional transmission electron microscopy. A change of the deformation mechanism from APB-coupled dislocation shearing to stacking fault shearing is found to depend on the strain rate. At lower strain rates, an increased stacking fault density is associated with a higher yield strength and higher work hardening rates at the early stages of plastic deformation due to a very high stacking fault density. After approximately 2.0 pct plastic strain, the stress reaches a plateau and decreases subsequently, which is associated with the formation and thickening of twins as shown by high-resolution scanning transmission electron microscopy. At higher strain rates, the work hardening rate is significantly lower in the early deformation stage. The role of segregation to planar defects and the influence of local phase transformations (LPT) at SESFs is further discussed in reference to the influence of the strain rate. The segregation of W as an η stabilizing element is found to be crucial for the formation of a local phase transformation in ERBOCo-4. At higher strain rates the phase transformation is hindered by insufficient W segregation, resulting in a higher twin density.

<https://doi.org/10.1007/s11661-023-06966-5>
© The Author(s) 2023

I. INTRODUCTION

SINCE the discovery of the metastable $L1_2$ -ordered $\text{Co}_3(\text{Al},\text{W})$ -Phase in the Co–Al–W system by Sato *et al.*^[1] in 2006, the promising properties of the novel Co-base superalloys caught a lot of attention. In comparison to Ni-base superalloys, the liquidus and solidus temperature of Co-base superalloys are higher^[2,3] and the as-cast condition shows less segregation.^[3] On the downside, ternary Co–Al–W alloys

exhibit a low solvus temperature, low phase stability, and poor oxidation resistance.^[2–4] Due to further developments of the alloy composition, the stability of the two-phase γ/γ' microstructure^[2,5,6] and oxidation resistance^[7–10] of Co-base superalloys has been improved significantly. For the widening of the γ/γ' region and an improved solvus temperature Ni^[5,11] is an essential element.

Co- and CoNi-base superalloys exhibit an interesting change in the defect structure which arises during constant strain rate experiments with increasing temperatures. While deformation in the γ matrix channels and shearing of the γ' -precipitates by anti-phase boundary (APB)-coupled dislocation pairs are dominant at lower temperatures,^[12–15] the dominant deformation mechanism at higher temperatures dependent on the alloy composition. Previous studies identified Ta as the crucial element, since it leads to a transition from shearing of γ' precipitates by APB-coupled dislocations to shearing under the formation of stacking faults (SF)^[6,14] presumably because Ta reduces the stacking fault energy (SFE).^[16] In contrast, the high temperature deformation mechanism of Ta-free alloys is the bowing

J. VOLLHÜTER, A. BEZOLD, M. KÖBRICH, M. GÖKEN, and S. NEUMEIER are with the Department of Materials Science & Engineering, Institute I: General Materials Properties, Friedrich-Alexander-Universität Erlangen-Nürnberg, Martensstraße 5, 91058 Erlangen, Germany. Contact e-mail: Jan.Vollhueter@fau.de N. KARPSTEIN, and E. SPIECKER are with the Institute of Micro- and Nanostructure Research (IMN) & Center for Nanoanalysis and Electron Microscopy (CENEM) & Interdisciplinary Center for Nanostructured Films (IZNF), Friedrich-Alexander-Universität Erlangen-Nürnberg, Cauerstraße 3, 91058 Erlangen, Germany. Manuscript submitted September 15, 2022; accepted January 12, 2023. Article published online February 10, 2023

and bypassing of matrix dislocations, which is associated with a decreasing flow stress.^[6,14,15,17] Systematic studies by Bezold *et al.* on a complex CoNi-base superalloy^[13] and a Co–Ti–Cr superalloy^[18] showed that in both alloys the transition from APB- to shearing under the formation of SFs results in an increase in work hardening. The change in deformation mechanisms was also associated with the diffusion lengths of Co and Cr, highlighting the role of segregation toward the planar defects.

The first indication of segregations to planar defects was a found increased z -contrast at a superintrinsic stacking fault (SISF),^[19] and a prove by EDS measurements was published in 2015.^[20] Due to the enrichments of segregating elements the energy of planar defects is reduced.^[21] Due to the enrichment of specific elements at the planar faults the composition shifts towards an energetically favorable phase like the γ -, $D0_{24}$ η - or $D0_{19}$ χ -phase. The γ -type segregations lead to an enrichment of Co and Cr and therefore a formation of a γ -like composition where at superextrinsic stacking faults (SESF) Shockley partial dislocations can shear on adjacent planes transforming the SESF into a micro twin.^[22–26] An increase of η -formers on the other hand leads to a local phase transformation which hinders the formation of twins and therefore exhibits superior mechanical properties.^[24,27–29] Even though the diffusion of specific elements is the determining step regarding segregation-assisted plasticity,^[30–32] the majority of investigated samples has been crept at higher temperatures and low strain rates which allows enough time for diffusion-controlled processes to take place. To evaluate the time depending step in the formation and propagation of stacking faults in superalloys, two different strain rates are used here to study the evolution of the defect structure at a temperature of 850 °C. Furthermore, the importance of local phase transformations at SESFs is discussed.

II. EXPERIMENTAL METHODS

The investigated single-crystalline CoNi-base superalloy named ERBOCo-4 (Co–32Ni–8Al–5.7W–2.8Ti–1.8Ta–6Cr–0.4Si–0.1Hf (at. pct))^[7] was cast in a laboratory-scale Bridgman furnace using a withdrawal rate of 3 mm/min with an estimated temperature gradient of 5 K/mm. The misorientation was measured by electron backscatter diffraction to be 4.3 deg from the [001] orientation using a *Nordlys2* detector from *Oxford instrument* in a *Zeiss Crossbeam 1540 EsB* scanning electron microscope (SEM). A heat treatment consisting of homogenization at 1280 °C for 8 hours and a two-step aging at 1050 °C for 5 and 9 hours at 900 °C was carried out. The γ' volume fraction and γ' precipitate size have been determined in a previous study^[13] and amount to 71 ± 2 pct and 437 ± 92 nm, respectively. The samples for the compression experiments were produced by wire electrical discharge machining with a diameter of 3 mm. Using a precision saw and subsequent grinding with up to 2500 grid SiC paper, a final height of 4.5 mm with plane-parallel faces with a

tolerance of less than 10 μm was adjusted. An *Instron 4505* electromechanical universal testing machine was used for the compression experiments with constant strain rates of 10^{-3} s^{-1} and 10^{-5} s^{-1} at a constant temperature of 850 °C. For the characterization of the defect structures, interrupted compression experiments between 0.2 and 14 pct plastic strain were carried out at each strain rate. TEM foils were cut perpendicular to the loading direction with a precision saw. Furthermore, [110]-oriented TEM foils were cut perpendicular to the dominant glide system which was detected using ECCI in the same SEM mentioned above. For certain conditions multiple TEM foils with different orientation were analyzed. The extracted TEM foils were ground to a thickness between 100 and 150 μm with up to 4000 SiC grid paper. For electrolytic thinning, a solution consisting of 16.7 pct nitric acid and 83.3 pct methanol was used in a *Struers Double Jet Tenupol-5* at -25 °C and 40 to 45 V. The defect structure was studied using a *Philips CM200* for the conventional TEM (CTEM) investigations. High-resolution scanning transmission electron microscopy (HRSTEM) was performed using a double aberration-corrected *Titan Themis*³ equipped with a Super-X energy-dispersive X-ray spectroscopy (EDS) detector at 300 keV. Integrated line scans of the HRSTEM-EDS mappings were obtained with the software *Velox* by *Thermo Fisher Scientific*. Center-of-symmetry (COS) analyses were carried out for a better visualization using a Python script analog to the Matlab scripts by Kovaric and Messé.^[19,33] To quantify the defect structure, 115 and 53 planar defects were analyzed on one TEM sample for the specimens with plastic deformation of 2 and 4 pct, respectively. Thermodynamic calculations were performed with the CALPHAD^[34,35] method, using the software *Thermo-Calc 21b* with the TCNI10 database.^[36]

III. RESULTS

A. Compression Experiments

The obtained true stress—true plastic strain diagrams for the two strain rates are shown in Figure 1(a), in which a clear dependence on the strain rate can be seen. Additionally, the work hardening rates for (a) are plotted in Figure 1(b), which are verified by further interrupted compression experiments. A lower strain rate leads to an increased work hardening in the early stages of plastic deformation which leads to a higher flow stress. After 1 pct plastic deformation the greatest difference in flow stress is present of approximately 100 MPa. At the same plastic deformation, the work hardening rate of the higher strain rate increases slightly, while the work hardening rate of the lower strain rate decreases rapidly. The work hardening rate becomes negative at 2 pct plastic deformation for the lower strain rate which marks the peak in flow stress as the flow stress decreases with further plastic deformation. Contrarily, the work hardening rate of the higher strain rate remains positive for the remaining plastic deformation of the compression test. To understand the

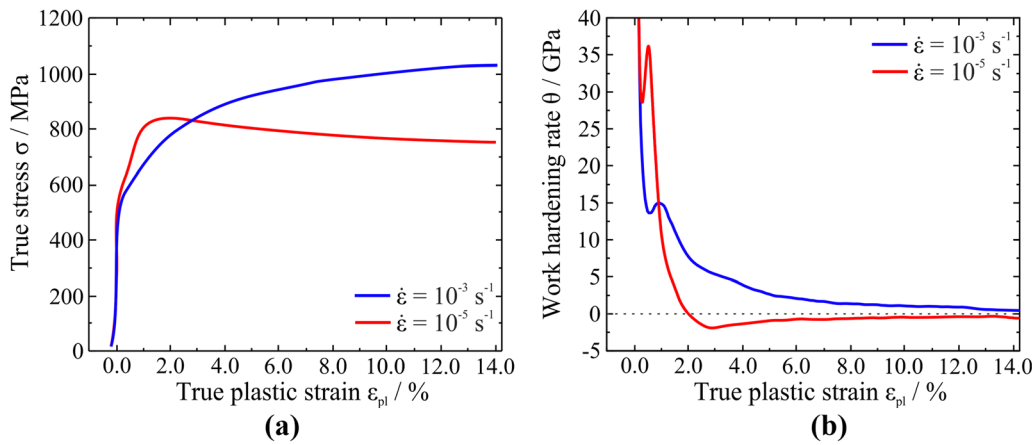


Fig. 1—(a) True stress—true plastic strain diagram and (b) work hardening for the two strain rates of 10^{-3} s^{-1} (blue) and 10^{-5} s^{-1} (red) at 850 °C (Color figure online).

difference in the work hardening rates, the defect structures at specific plastic strains are further analyzed.

B. Characterization of the Defect Structure

Figure 2(a) shows the true stress—true plastic strain diagram of the interrupted specimens after a plastic deformation of approximately 0.2 pct. Even though the deviation of the different curves is marginal, the resulting defect structures in Figures 2(b) through (e) are clearly different from each other. The defect structure of the sample deformed with a strain rate of 10^{-3} s^{-1} is dominated by γ matrix dislocations and the shearing of γ' precipitates by APB-coupled dislocations, which mainly form Kear–Wilsdorf locks (KWL) (Figure 2(c)). The slower deformed sample (strain rate 10^{-5} s^{-1}) exhibits a defect structure dominated by stacking faults as shown in Figure 2(e). Furthermore, APB-coupled dislocations, which form KWL in the precipitates, are occasionally observed. For both

conditions, the defect structure is highly inhomogeneous and areas with no or minor plastic deformation are present (see Figures 2(b) and (d)).

The true stress—true plastic strain diagrams of the interrupted samples at 1 pct plastic deformation are shown in Figure 3(a) and reveal a difference in the stress of about 100 MPa. For the sample deformed with a strain rate of 10^{-3} s^{-1} , the defect mechanisms are unaffected by the additional plastic deformation, but the defect density increases significantly (Figure 3(b)). The dominant deformation mechanisms are still dislocation activity in the γ matrix channels and the cutting of γ' precipitates by APB-coupled dislocations. Occasionally cutting under the formation of stacking faults is observed. Additionally, Figure 3(c) shows glide bands of mobile APB-coupled dislocations. However, such glide bands are only infrequently observed across the defect structure. The stacking fault density of the sample deformed at lower strain rate of 10^{-5} s^{-1} to 1 pct plastic strain increases extremely in comparison to the sample

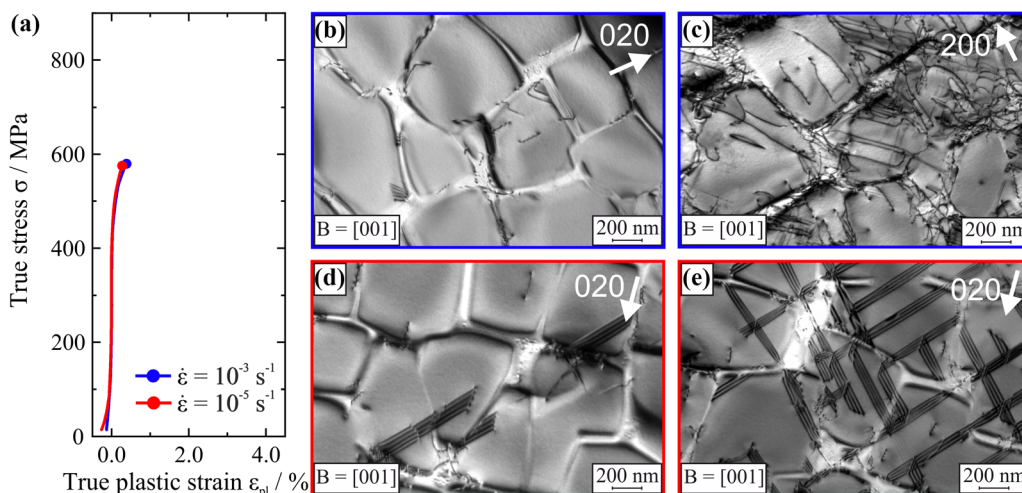


Fig. 2—Defect structures after 0.2 pct plastic deformation. (a) True stress—true plastic strain curves for different strain rates. Corresponding defect structure at a strain rate of (b, c) 10^{-3} s^{-1} and (d, e) 10^{-5} s^{-1} . BF images were taken in two-beam conditions close to the [001] zone axis.

deformed to 0.2 pct (Figures 3(d) and (e)). In general, the homogeneity of plastic deformation increases at a plastic strain of 1 pct, although occasionally shear bands are observed as shown in Figure 3(e). The stacking faults are mainly edge-on, which indicates that two glide systems are dominant (Figure 3(e)). Due to the increasing stacking fault density, the number of interactions between stacking faults also increases strongly. The presence of twins is indicated by the appearance of additional spots on the diffraction pattern, as shown in Figure 3(e).

After 2 pct plastic strain, the difference of the maximum stress decreases, which is shown in the stress–strain diagram in Figure 4(a). The stacking fault density of the samples deformed at the higher strain rate

increases which is shown in Figures 4(b) and (c), while APB-coupled dislocations, which form KWLs in the precipitates, are still present in great number. The newly formed stacking faults extend on average over one or two precipitates, with stacking faults located on all four octahedral planes (Figure 4(c)). The already high stacking fault density of the sample deformed with the lower strain rate of 10^{-5} s^{-1} increases further after the additional plastic deformation (Figure 4(d)). An additional spot in the diffraction pattern indicates the presence of twins, as shown in Figure 3(d). Figure 4(e) shows the existence and formation of extensive glide bands with an extreme planar fault density.

After deformation of 4 pct, the stress in the sample deformed with a strain rate of 10^{-3} s^{-1} is higher than

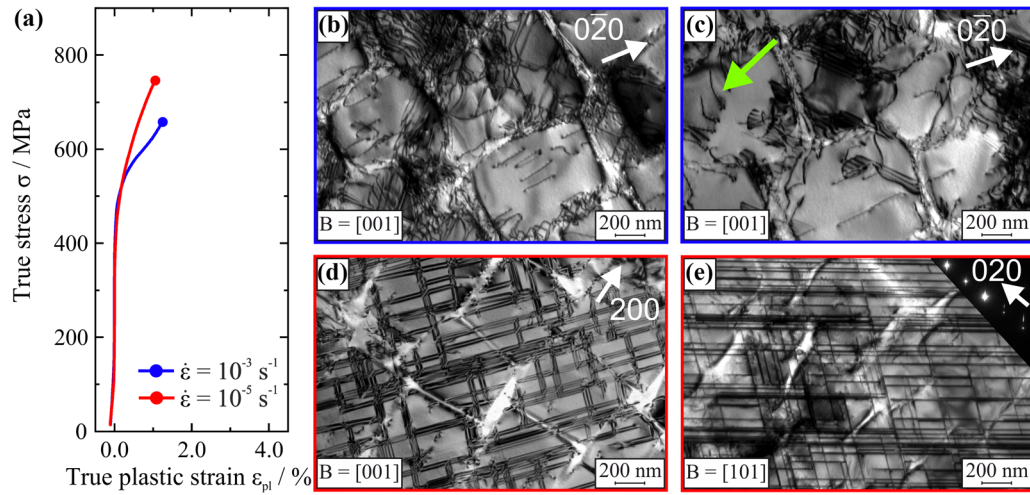


Fig. 3—Defect structures after 1 pct plastic deformation. (a) True stress—true plastic strain curves for different strain rates. Corresponding defect structure at a strain rate of (b, c) 10^{-3} s^{-1} and (d, e) 10^{-5} s^{-1} . A shear band of APB-coupled dislocations is marked with a green arrow in (c). Presence of twins is shown by the inset of the diffraction pattern showing additional twinning spots in (e). All BF images were taken in two-beam conditions close to the [001] zone axis, except for (e) which was taken close to the [101] zone axis (Color figure online).

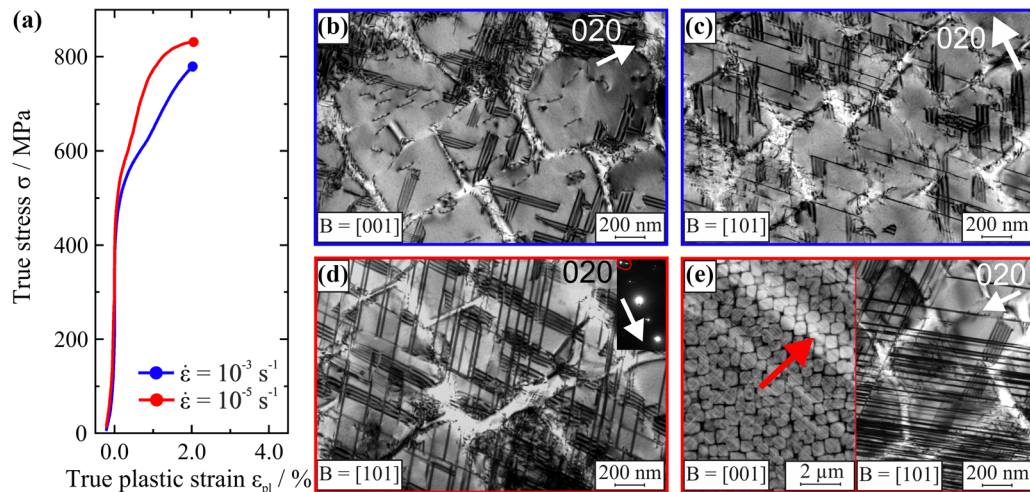


Fig. 4—Defect structures after 2 pct plastic deformation. (a) True stress—true plastic strain curves for different strain rates. Corresponding defect structure at a strain rate of (b, c) 10^{-3} s^{-1} and (d, e) 10^{-5} s^{-1} . (d) Presence of twins is shown by the inset of the diffraction pattern showing additional twinning spots. (e) The presence of shear bands are revealed by ECCI-contrast and marked with a red arrow. TEM-images of a shear band shows the extreme high stacking fault density. All BF images were taken in two-beam conditions close to the [101] zone axis, except for (b) which was taken close to the [001] zone axis (Color figure online).

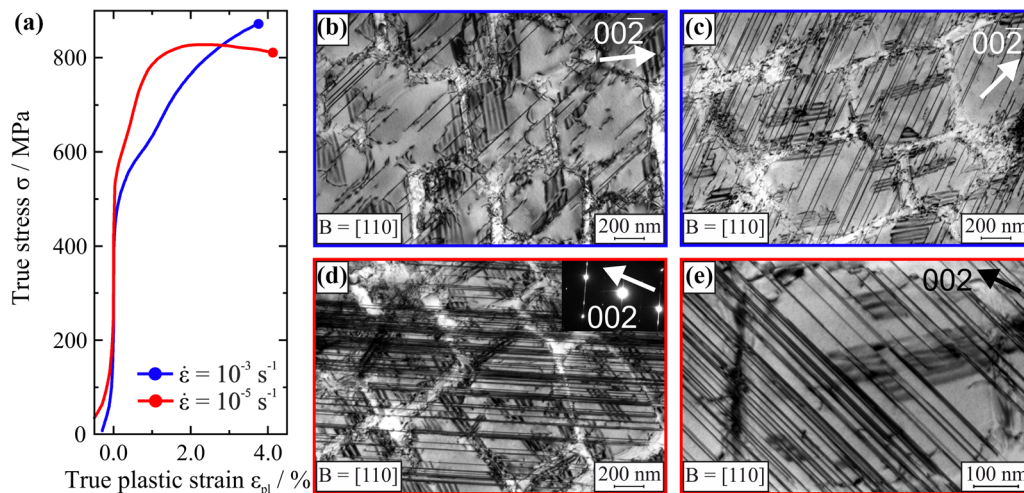


Fig. 5—Defect structures after 4 pct plastic deformation. (a) True stress—true plastic strain curves for different strain rates. Corresponding defect structure at a strain rate of (b, c) 10^{-3} s^{-1} and (d, e) 10^{-5} s^{-1} . (d) Presence of twins is shown by the inset of the diffraction pattern showing additional twinning spots. All BF images were taken in two-beam conditions close to the [110] zone axis.

that one of the sample tested with a strain rate of 10^{-5} s^{-1} as shown in Figure 5(a). APB-coupled dislocations are observed in the γ' precipitates which can be seen in Figure 5(b). The stacking fault density increases while the APB-density decreases in comparison with the previously presented conditions tested at a strain rate of 10^{-3} s^{-1} . Figure 5(c) shows the dominance of one glide system. The defect structure of the sample deformed with a strain rate of 10^{-5} s^{-1} shows only slight deviations from the previously presented condition at 2 pct plastic deformation. Clear additional spots, caused by the formation and thickening of twins, are present in the diffraction pattern as shown by the inset in Figure 5(d). The localization of plastic deformation in glide bands is shown in Figure 5(d).

C. Atomic-Scale Characterization of the Planar Faults

For a better understanding of the observed defect structures, the samples deformed at a strain rate of 10^{-5} s^{-1} to a plastic strain level of 2 and 4 pct are further

analyzed by HRSTEM in [110] direction. The defect structure of the sample after a plastic strain of 2 pct consists mainly of SISFs, SESFs and micro-twins. Interestingly, the predominantly occurring twin configuration is a three-layered twin. This configuration has also been observed previously in a Ni-base superalloy.^[37] Figure 6(a) shows a HAADF image and the corresponding COS image of two three-layered twins. A transition from a single-layer SISF to the three-layered twin is observable, which converts into a two-layer SESF (Figure 6(b)). Additionally, a grid-like pattern appears at a majority of the SESF which is an indication of a local η phase transformation.^[28] Figure 6(c) shows an SESF with local η phase transformation where the grid-like pattern is indicated in the inset. Even though the grid-like pattern does not appear continuously along the SESFs, a regular re-appearing is observed. Additionally, a local phase transformation is also present in a sample deformed at the same strain rate of 10^{-5} s^{-1} at the same temperature to a plastic deformation of 1 pct (Figure 6(d)).

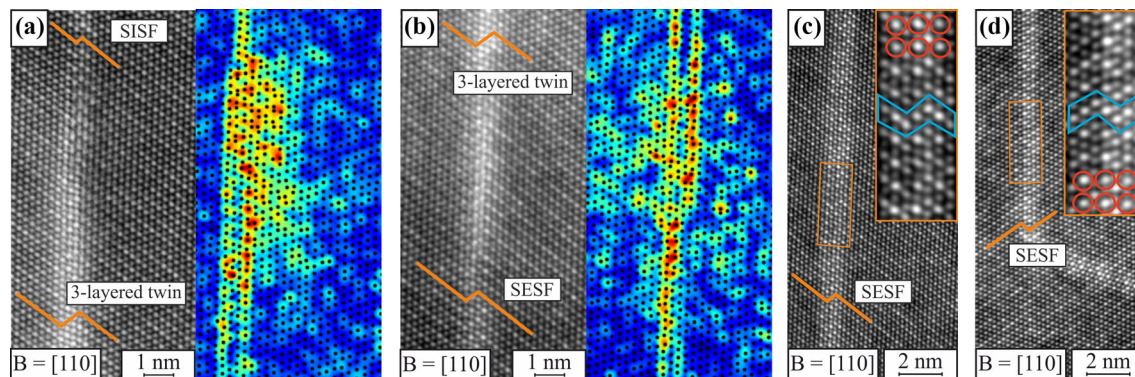


Fig. 6—Defect structure after 2 pct plastic strain at a strain rate of 10^{-5} s^{-1} and a temperature of 850 °C: (a) HRSTEM image and corresponding COS-image of the transition of a SISF into a three-layered twin. (b) HRSTEM image and corresponding COS-image of the transition of a three-layered twin into an SESF. (c) Local η phase transformation as characterized by a grid-like pattern as shown in the inset by the red circles although it is not continuous as indicated by the blue box. (d) Local η phase transformation after plastic deformation of 1 pct at a strain rate of 10^{-5} s^{-1} . The stacking sequent is indicated by the orange lines across the planar defects (Color figure online).

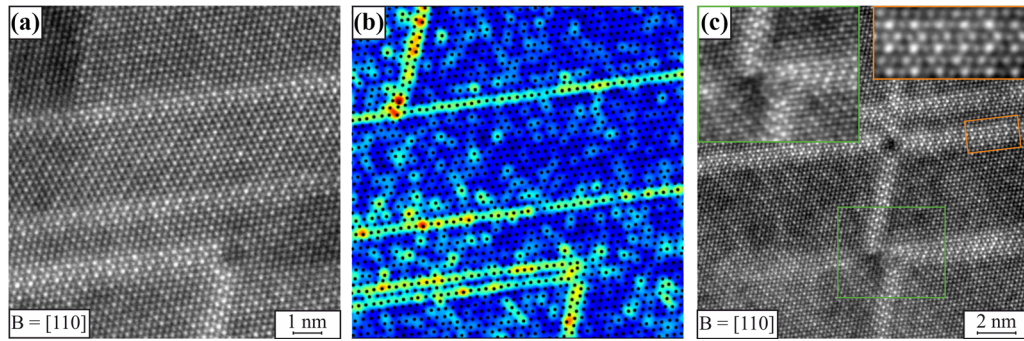


Fig. 7—Defect structure after 4 pct plastic deformation at a strain rate of 10^{-5} s^{-1} : (a, b) HRSTEM image and corresponding COS-image a twin with 16 layers and an L-Type interaction of a SISF and a SESF. (c) Two defect interactions between a SESF and a SISF, three-layered twin and a SISF which is shown magnified in the green inset. Formation of a local phase transformation is highlighted in the orange inset (Color figure online).

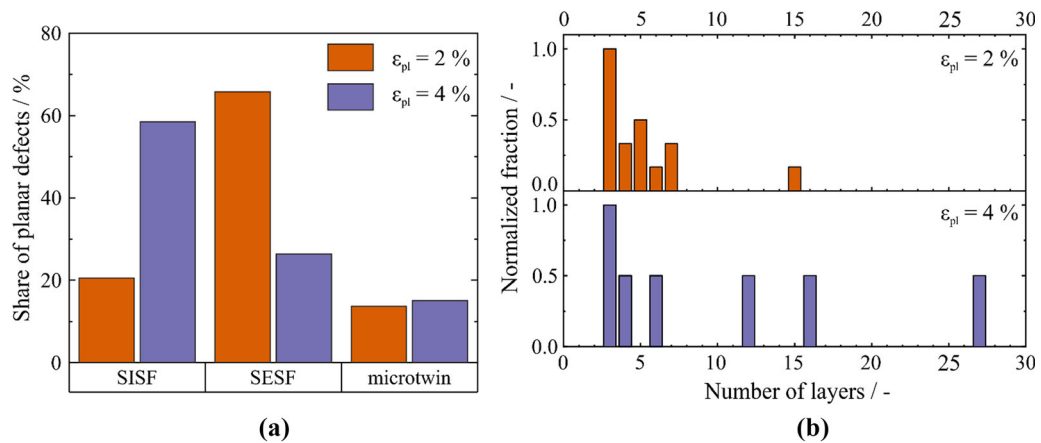


Fig. 8—(a) Share of SISFs, SESFs, and microtwins and (b) distribution of the layer number of the microtwins for both conditions. Note that the graph in (b) is normalized to the highest occurring number of layers.

The HRSTEM investigations of the 4 pct deformed sample at a strain rate of 10^{-5} s^{-1} reveal an increased twin thickness. Figures 7(a) and (b) shows a twin with 16 layers in addition to an L-type interaction of an SESF and a SISF with a reduced z -contrast at the interaction. Furthermore, at the SESFs a local phase transformation is observable and highlighted in Figure 7(c). Additionally, several different interactions of planar defects are shown in the same image. Interestingly, only the same SISF is sheared by two SESFs with only one interaction showing a reduced z -contrast. The interaction of a SISF and a three-layered twin shows a clearly reduced z -contrast. The SISF exhibits a displacement of 6 atomic layers, which is likely due to the interaction with the three-layered twin.

A detailed HRSTEM quantification of the defect structure is presented in Figure 8 for the conditions deformed at a strain rate of 10^{-5} s^{-1} up to a plastic strain of 2 and 4 pct. The fractions of SESFs and SISFs change significantly with further plastic deformation, while the fraction of twins stays constant. Figure 8(b) shows the distribution of the number of layers of the analyzed twins. At a plastic strain of 2 pct, the average

twin size is approximately 5 layers with a significant fraction of three-layered twins. Further plastic deformation increases the average twin size to 10 layers. Individual twins expand significantly and display a high number of layers as other twins do not thicken at all. Interestingly, the share of SISFs rises to 58.5 pct as the percentage of SESFs drops to 26.4 pct whereas after 2 pct plastic deformation the fraction of SESFs amounts to 65.8 pct and the fraction of SISFs to 20.5 pct.

Additional STEM-EDS measurements were conducted on planar defects of the 4 pct deformed sample to further analyze the role of segregation towards the planar defects. The measured chemical compositions of the γ' phase and the investigated planar defects are listed in Table I. Figure 9(a) shows the investigated twin and SESF, where the enlarged area from the measuring range shows the grid-like pattern of a local η phase transformation. The twin boundaries display an asymmetrical segregation profile, which has already been observed for thicker twins.^[38] While the overall segregation tendencies for both twin boundaries are similar, specific elements show slightly different segregation magnitudes. The magnitude of depletion or enrichment

Table I. Measured Composition of the Analyzed Planar Defects and the Surrounding γ' -Phase in At. Pct

	Co	Ni	Al	W	Ti	Ta	Cr
γ' Phase	38.6 ± 0.4	38.1 ± 0.4	8.1 ± 0.1	5.1 ± 0.1	4.1 ± 0.1	2.3 ± 0.1	3.6 ± 0.1
TB1	41.8 ± 0.0	34.7 ± 0.4	7.0 ± 0.2	5.6 ± 0.2	4.1 ± 0.1	2.6 ± 0.1	4.2 ± 0.1
TB2	41.7 ± 0.3	35.0 ± 0.3	7.1 ± 0.2	5.5 ± 0.1	3.7 ± 0.1	2.3 ± 0.1	4.7 ± 0.1
SESF	43.0 ± 0.2	33.0 ± 0.4	6.3 ± 0.2	6.7 ± 0.1	4.3 ± 0.2	2.8 ± 0.2	4.1 ± 0.1
Three-Layered Twin	44.6 ± 0.3	31.6 ± 0.3	6.0 ± 0.1	7.2 ± 0.2	4.0 ± 0.1	2.1 ± 0.1	4.6 ± 0.1

Hf and Si are not included as their concentration is too low for EDS measurements. The concentration of the planar defects was determined by averaging along the planar fault and then take the peak value.

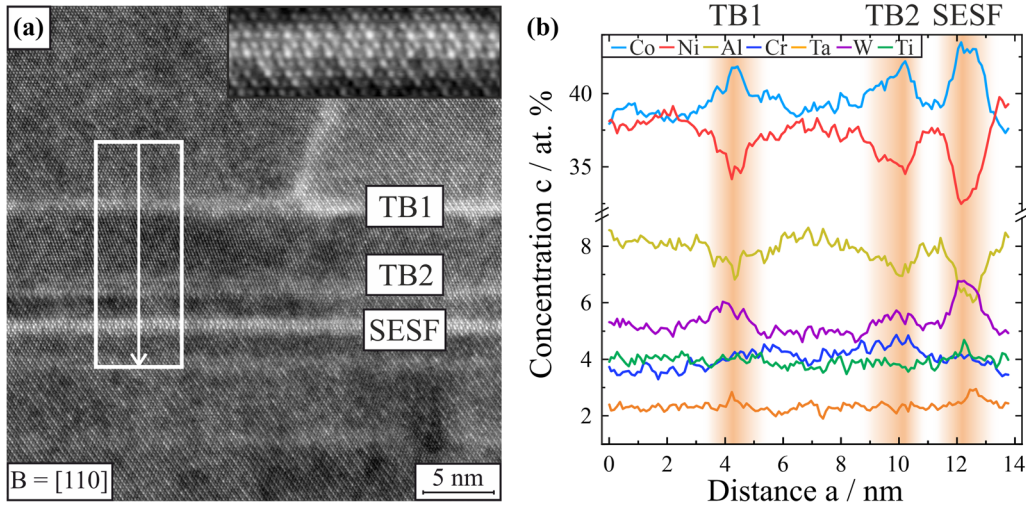


Fig. 9—(a) EDS analysis of a twin and an SESF with local phase transformation after a plastic deformation of 4 pct at a strain rate of 10^{-5} s^{-1} . (b) Vertically integrated EDS line profile from the region marked in (a) along the direction of the arrow.

of Co, Ni, Al, and Ti is similar for both twin boundaries, with Cr enriched throughout the microtwin but more strongly segregating toward TB2. In contrast, W segregates more strongly toward TB1. Ta also shows a slight enrichment in TB1, although this peak is not distinct enough to be interpreted as a clear segregation. The magnitude of segregation is significantly higher for the SESF in comparison to the twin boundaries in accordance with previous results.^[13,39] The W and Co concentration increases significantly at the SESF. Additionally, Ta is also segregating towards the planar fault, while Al and Ni are depleted.

Since three-layered twins occur quite frequently, the segregation profile of such a defect has been analyzed for the first time to the authors' knowledge. The area of the vertical integration profile and the chemical composition throughout the planar defect is shown in Figures 10(a) and (b) respectively. The segregation tendency is consistent with the previously presented segregation behavior of the twin boundaries and SESF, while the magnitude of segregation is significantly higher. W, Cr, and Co segregate strongly towards the planar defect while Al and Ni are depleted. Ta and Ti show no segregation tendency over the planar defect.

IV. DISCUSSION

The detailed CTEM investigations conducted on samples deformed with different strain rates at a constant temperature revealed that the transition from cutting the precipitates by APB-coupled dislocations to shearing under the formation of stacking faults is not only observed with increasing temperature as known from literature^[13,18] but also with decreasing strain rate.

In the following the influence of the strain rate on the formation of a local η phase transformation and the effects on the mechanical properties are discussed. The occurrence of the different planar faults in dependence on the plastic strain is debated. Finally, the evolution of the defect structure is analyzed and associated with the mechanical behavior.

A. Influence of Local Phase Transformation

As mentioned before, a grid-like pattern was observed at the SESFs investigated in this study which was highlighted in Figures 6 and 7, indicating a local η phase transformation along these faults.^[24,28] However, this local phase transformation does not occur continuously

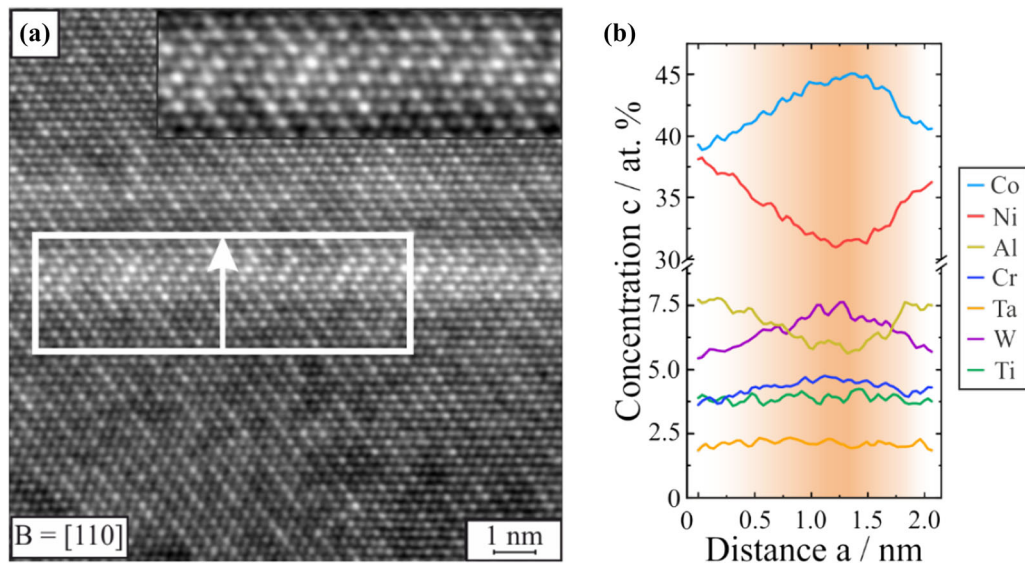


Fig. 10—EDX: (a) Three-layered twin observed in a specimen after a plastic deformation of 4 pct at a strain rate of 10^{-5} s^{-1} . (b) Vertically integrated EDS line profile from the region marked in (a) along the direction of the arrow.

along the entire length of the SESF. In a previous study,^[13] in which the same superalloy ERBOCo-4 was analyzed after 1 pct plastic deformation at a strain rate of 10^{-4} s^{-1} and the same temperature of 850 °C, no grid-like pattern was observed at the SESFs, with the superlattice contrast being well visible in both samples. Heavy elements such as Ta and W stabilize the $D0_{24}$ crystal structure with order preferences toward the Wyckoff 2a atomic positions, resulting in the grid-like pattern due to the increased z -contrast.^[24] Consequently, the occurrence of such a lattice-like pattern in combination with an enrichment of η -stabilizing elements is indicative of a local phase transformation. For both SESFs, the composition across the planar fault has been determined and the difference in comparison with the initial composition of the γ' phase is shown in Table II. As mentioned above, especially the concentration of the refractory metals W and Ta are important as they strongly stabilize the η phase in CoNi-base superalloys.^[27] The SESF from this study which shows an η phase transformation has a significantly increase of the W content of 1.6 at. pct compared to 0.6 pct at the SESF without a local η phase transformation in respect to the W content of the surrounding γ' -phase. Due to the significantly stronger enrichment of η stabilizing elements and the present grid-like pattern, it becomes

evident that a partially local phase transformation is present in the investigated sample, which was deformed with a strain rate of 10^{-5} s^{-1} , whereas the faster deformed sample does not show a pronounced local phase transformation. This raises the question of why the phase transformation does not occur at strain rates of 10^{-4} s^{-1} and only partially at strain rates of 10^{-5} s^{-1} .

The composition of both specimens of the same superalloy ERBOCo-4 that come from two different castings shows only a slight deviation (see Table II) in the Ta and W content which both stabilize the η phase in CoNi-base superalloys according to Smith *et al.*^[27] To exclude the influence of the composition on the formation of a LPT, thermodynamic calculations were performed after Feng *et al.*^[40] The calculations of the free Gibbs energy resulted in equal energies for the phases $D0_{24}$, $L1_2$, and hcp. Therefore, in this specific case, the influence of the composition on whether a phase transformation occurs can be excluded as a decisive factor. Even though no detailed study on the microstructure of the sample that was deformed to 1 pct at a strain rate of 10^{-5} s^{-1} was performed, a LPT was observed at all SESFs. Therefore, the plastic strain is also not the deciding factor for the formation of LPTs, which leaves the different strain rates as the remaining factor. The diffusion of W has already been identified as

Table II. Measured Composition of the γ' -Phase and the Change in the Composition of the Analyzed SESFs Relative to the γ' Phase in ERBOCo-4 from This Work and Bezold *et al.*^[13]

	Co	Ni	Al	W	Ti	Ta	Cr
γ' Phase	38.4	38.4	8.07	5.1	4.2	2.3	3.6
Δ SESF with LPT	+ 4.6	- 5.3	- 1.8	+ 1.6	+ 0.2	+ 0.4	+ 0.5
γ' Phase ^[13]	38.7	37.6	7.4	4.4	4.4	3.2	3.4
Δ SESF Without LPT ^[13]	+ 3.9	- 4.1	- 1.6	+ 0.6	+ 0.2	+ 0.2	+ 0.8

Values in at. pct.

the rate-determining step for the segregation-assisted propagation of the leading partials of SISFs and SESFs.^[30,31] The strong segregation of W towards the SESF with a local η phase transformation suggests that W plays a key role in the formation of this phase transformation, which is in accordance with DFT calculations by Smith *et al.*^[27] This suggests that due to the slow diffusivity of W, a local η phase transformation at SESFs is impeded if the required W segregation cannot be achieved in the short experiment time. The discontinuous formation of the η phase at SESFs is also the result of insufficient diffusion of η stabilizing elements towards the planar defect. However, this can also be influenced by local concentration fluctuations. In contrast, lower strain rates and thus longer times for diffusion enable accumulation of a higher concentration of W and therefore promote the formation of a local η phase transformation at planar faults. Accordingly, the majority of SESFs display LPTs at lower strain rates. SESFs, which show no LPT, however, can transform into twins which then expand further. The asymmetric segregation profile indicates the preferred shearing of twinning partial dislocation on one side of the twin, which is indicated by higher concentrations of Co and Cr at one twin boundary. The concentration of Co and Cr increases through the shearing of a twinning partial dislocation, which lowers the energy barrier for further shearing at this twin boundary. The preferred shearing of partial dislocations at one twin boundary seems to be a self-reinforcing effect. At higher strain rates the insufficient formation of LPTs at SESFs does not raise the energy barrier high enough to prevent Shockley partial dislocations to convert the SESFs into a microtwin which leads to a higher twin density.

B. Quantification of Planar Defects

The distribution of SESFs and SISFs changes significantly as a function of plastic strain. The increasing number of SISFs is unexpected, as SESFs should be the dominant planar defect for compression experiments of [001] oriented samples.^[41,42] The HRSTEM analysis showed especially in the later deformation progress many defect interactions, which include many cross-slip events with SISFs involved. One possible reason for the high number of observed SISFs are the complex interactions of numerous planar defects and the cross slipping of SISFs as described by Lu *et al.*^[43] Even though not directly observed, the nucleation of stacking faults from twin boundaries as described by Freund *et al.*^[26] could further impact the defect structure.

The share of twins stays approximately equal from plastic deformation of 2 to 4 pct. The reason for this could be an overall increasing defect density, where the number of twins grows at the expense of the number of SESFs. This is underlined through the steady percentage of twins shown in Figure 8(a). However, no significant increase in defect density was observed in the CTEM investigations due to the increase in plastic deformation. Additionally, the number of layers in the existing twins increases significantly with further plastic deformation (Figure 8(b)) which leads to a softening of the material

due to the high contribution of twins to the plastic deformation. The unusual high number of SISF of over 60 pct for a [001] oriented sample deformed under compression is yet not fully understood. This could be a result of multiple stacking fault interactions which lead to cross-slip events like described by Lu *et al.*^[43] For a better understanding of the defect structure at higher plastic strains more HRSTEM investigations are necessary. A similar defect structure has also been observed after creep experiments for the same superalloy, where a low number of twins exhibits large numbers of layers.^[44]

The regular appearance of three-layered twins in the 2 and 4 pct deformed samples at 850 °C and a strain rate of 10^{-5} s^{-1} is not fully understood yet. The magnitude of segregation of the three-layered twin exceeds both the twin boundaries and the SESF suggesting a high energy fault. For SISFs, SESFs and twin boundaries local phase transformations are known.^[21,24,28,31,38,45,46] The high magnitude of segregation and the high z -contrast could be an indication of a local phase transformation at the three-layered twins as well. Nevertheless, the formation of these planar defects is still unknown and requires more investigation on this topic.

C. Evolution of the Defect Structure

A schematic drawing of the evolution of the defect structure as a function of strain rate and plastic strain is shown in Figure 11. The defect structure at the initial

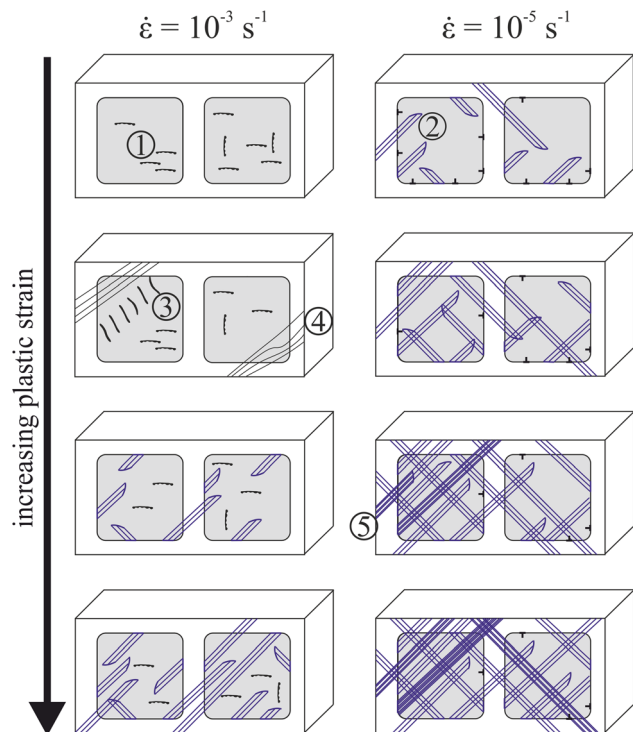


Fig. 11—Schematic showing the defect evolution with increasing plastic strain at different strain rates. The schematic defect structures represent: (1) APB-coupled dislocation pair, cross slipped on (100) plane; (2) Stacking fault; (3) mobile APB-coupled dislocation pair; (4) Matrix dislocations; (5) Microtwin. Note that the defect structure is projected of the [001]-direction.

yielding stage consists of mainly sessile APB-coupled dislocation pairs for the faster deformed and stacking faults for the slower deformed sample. This crucial difference in the defect structure highlights the strain rate as a major factor on the transition of the deformation mechanisms. The general absence of stacking faults in the early stages of deformation of the samples deformed with the higher strain rate of 10^{-3} s^{-1} suggests that not only the propagation but also the formation of stacking faults is a diffusion-controlled process. Since diffusion processes are required for the formation and propagation of stacking faults, the deformation for the faster deformed sample in the initial stage of yielding is based on the athermal cutting of APB-coupled dislocation pairs and the Orowan process. Other deformation mechanism, such as the shearing of a single superpartial dislocation that generates an APB in its path, are observed only at higher temperatures due to their high fault energy.^[13] Only when the strain rate is lowered or the plastic deformation progresses, *i.e.*, more time for diffusion processes is available, these segregation-assisted mechanisms start to occur. Later in the deformation process, as the shearing under the formation of stacking faults is the dominant deformation mechanism, the propagation velocity of stacking faults is an important factor for the amount of plastic deformation that they can contribute to the overall plastic deformation. The segregation towards the stacking faults is here the rate depending step for the propagation, but also for the shearing of other stacking faults. Atomistic phase field simulations by Lilenstein *et al.*^[29] show a significant influence of the defect velocity on the segregation profile, which was later experimentally verified by Wu *et al.*^[47] At lower strain rates, due to increased time for diffusion, the transition to shearing under the formation of stacking faults is promoted. Additionally, further plastic deformation leads also to an increased stacking fault density and thus, large work hardening rates at the early stages of plastic deformation. Later in the deformation process, the work hardening rate decreases and shifts to negative values. Due to the low strain rate, the time for diffusion is two orders of magnitude higher for the samples deformed with a strain rate of 10^{-5} s^{-1} . Hence, the diffusion-controlled cutting of γ' precipitates under the formation of stacking faults is already the dominant deformation mechanism at a plastic strain of 0.2 pct. The occurring anomalous work hardening behavior has already been linked to stacking fault shearing and the interaction of stacking faults.^[13,18] Due to the increasing stacking fault density with further plastic deformation, the interaction of stacking faults rises, and obstacles for further propagation, which requires additional segregation towards the interaction, are created.^[39,43,48] At the higher strain rate, the dominant cutting mechanism remains shearing by APB-coupled dislocations, where shear bands of mobile APB-coupled dislocations are present. These shear bands were only observed in the sample deformed to a plastic strain of 1 pct, which does not rule out their existence in the other conditions deformed at the higher strain rate. With further plastic deformation, more time for diffusion is available which enables the segregation-assisted nucleation of stacking faults. The influence of not only the temperature,^[13] but

also the time has been shown in this study as an important factor for the transition towards shearing under the formation of stacking faults. This is evident in the increasing stacking fault density and a transition in the deformation mechanism after a plastic deformation of 2 pct at the higher strain rate. Due to the formation and thickening of twins, which is in detail discussed in Section IV-B, the work hardening of the samples deformed with the slower strain rate is stagnating and finally, the material softens. The reduced energy barrier for Shockley partial dislocations to shear the γ' precipitates at adjacent planes is the main reason for the reduced strength.^[22-24,26,31] While the thickening of twins at the sample deformed with the lower strain rate leads to negative work hardening rates, the increasing stacking fault density leads to higher work hardening rates for the higher strain rate.

V. SUMMARY AND CONCLUSION

The deformation behavior of the single-crystal Co-Ni-base superalloy ERBOCo-4 (Co-32Ni-8Al-5.7W-2.8Ti-1.8Ta-6Cr-0.4Si-0.1Hf) deformed at 850 °C at varying strain rates and plastic strains has been investigated by conventional, high-resolution and analytical (S)TEM. The following conclusions can be drawn:

- A strain rate dependent transition from cutting of the γ' precipitates by APB-coupled dislocation pairs to shearing under the formation of stacking faults is found.
- Stacking fault shearing leads to higher work hardening rates in the early stages of plastic deformation. Formation and thickening of twins lead to a peak of strength at about 2 pct plastic strain and subsequent softening.
- Local η phase transformation of the SESFs prevents the majority of the faults from transforming into microtwins.
- Segregation of slowly diffusing η stabilizing elements such as W seems to be the rate-determining step in the formation of local phase transformations.

ACKNOWLEDGMENTS

The authors acknowledge funding by the Deutsche Forschungsgemeinschaft (DFG) through projects B3, A7 and Z01 of the Collaborative Research Center SFB/TR 103: “From Atoms to Turbine Blades—A Scientific Approach for Developing the Next Generation of Single Crystal Superalloys”.

FUNDING

Open Access funding enabled and organized by Projekt DEAL.

CONFLICT OF INTEREST

The authors declare that they have no known competing financial interests or personal relationships that could have appeared to influence the work reported in this paper.

OPEN ACCESS

This article is licensed under a Creative Commons Attribution 4.0 International License, which permits use, sharing, adaptation, distribution and reproduction in any medium or format, as long as you give appropriate credit to the original author(s) and the source, provide a link to the Creative Commons licence, and indicate if changes were made. The images or other third party material in this article are included in the article's Creative Commons licence, unless indicated otherwise in a credit line to the material. If material is not included in the article's Creative Commons licence and your intended use is not permitted by statutory regulation or exceeds the permitted use, you will need to obtain permission directly from the copyright holder. To view a copy of this licence, visit <http://creativecommons.org/licenses/by/4.0/>.

REFERENCES

1. J. Sato, T. Omori, K. Oikawa, I. Ohnuma, R. Kainuma, and K. Ishida: *Science*, 2006, vol. 312, pp. 90–91.
2. A. Bauer, S. Neumeier, F. Pyczak, and M. Göken: *Scripta Mater.*, 2010, vol. 63, pp. 1197–1200.
3. T.M. Pollock, J. Dibbern, M. Tsunekane, J. Zhu, and A. Suzuki: *JOM*, 2010, vol. 62, pp. 58–63.
4. L. Klein, A. Bauer, S. Neumeier, M. Göken, and S. Virtanen: *Corros. Sci.*, 2011, vol. 53, pp. 2027–34.
5. C.H. Zenk, S. Neumeier, N.M. Engl, S.G. Fries, O. Dolotko, M. Weiser, S. Virtanen, and M. Göken: *Scripta Mater.*, 2016, vol. 112, pp. 83–86.
6. A. Suzuki and T.M. Pollock: *Acta Mater.*, 2008, vol. 56, pp. 1288–97.
7. N. Volz, C.H. Zenk, R. Cherukuri, T. Kalfhaus, M. Weiser, S.K. Mäkinen, C. Betzing, M. Lenz, B. Gault, S.G. Fries, J. Schreuer, R. Vaßen, S. Virtanen, D. Raabe, E. Spiecker, S. Neumeier, and M. Göken: *Metall. Mater. Trans. A*, 2018, vol. 49A, pp. 4099–4109.
8. S. Neumeier, L.P. Freund, and M. Göken: *Scripta Mater.*, 2015, vol. 109, pp. 104–07.
9. L. Klein, M.S. Killian, and S. Virtanen: *Corros. Sci.*, 2013, vol. 69, pp. 43–49.
10. L. Klein, Y. Shen, M.S. Killian, and S. Virtanen: *Corros. Sci.*, 2011, vol. 53, pp. 2713–20.
11. K. Shinagawa, T. Omori, J. Sato, K. Oikawa, I. Ohnuma, R. Kainuma, and K. Ishida: *Mater. Trans.*, 2008, vol. 49, pp. 1474–79.
12. A. Suzuki, G.C. DeNolf, and T.M. Pollock: *Scripta Mater.*, 2007, vol. 56, pp. 385–88.
13. A. Bezold, N. Volz, M. Lenz, N. Karpstein, C.H. Zenk, E. Spiecker, M. Göken, and S. Neumeier: *Acta Mater.*, 2022, vol. 227, p. 117702.
14. Z. Fan, C. Wang, C. Zhang, Y. Yu, H. Chen, and Z. Yang: *Mater. Sci. Eng. A*, 2018, vol. 735, pp. 114–20.
15. L. Shi, J.J. Yu, C.Y. Cui, and X.F. Sun: *Mater. Sci. Eng. A*, 2015, vol. 620, pp. 36–43.
16. N. Volz, F. Xue, C.H. Zenk, A. Bezold, S. Gabel, A.P.A. Subramanyam, R. Drautz, T. Hammerschmidt, S.K. Mäkinen, B. Gault, M. Göken, and S. Neumeier: *Acta Mater.*, 2021, vol. 214, p. 117019.
17. Z. Fan, X. Wang, Y. Yang, H. Chen, Z. Yang, and C. Zhang: *Mater. Sci. Eng. A*, 2019, vol. 748, pp. 267–74.
18. A. Bezold, N. Volz, M. Lenz, C.H. Zenk, E. Spiecker, M. Mills, M. Göken, and S. Neumeier: *Scripta Mater.*, 2021, vol. 200, p. 113928.
19. V.A. Vorontsov, L. Kovarik, M.J. Mills, and C.M.F. Rae: *Acta Mater.*, 2012, vol. 60, pp. 4866–78.
20. G.B. Viswanathan, R. Shi, A. Genc, V.A. Vorontsov, L. Kovarik, C.M.F. Rae, and M.J. Mills: *Scripta Mater.*, 2015, vol. 94, pp. 5–8.
21. M.S. Titus, Y.M. Eggeler, A. Suzuki, and T.M. Pollock: *Acta Mater.*, 2015, vol. 82, pp. 530–39.
22. D. Barba, S. Pedrazzini, A. Vilalta-Clemente, A.J. Wilkinson, M.P. Moody, P.A.J. Bagot, A. Jérusalem, and R.C. Reed: *Scripta Mater.*, 2017, vol. 127, pp. 37–40.
23. T.M. Smith, R.R. Unocic, H. Deutchman, and M.J. Mills: *Mater. High Temp.*, 2016, vol. 33, pp. 372–83.
24. T.M. Smith, B.D. Esser, N. Antolin, A. Carlsson, R.E.A. Williams, A. Wessman, T. Hanlon, H.L. Fraser, W. Windl, D.W. McComb, and M.J. Mills: *Nat. Commun.*, 2016, vol. 7, p. 13434.
25. Y.M. Eggeler, J. Müller, M.S. Titus, A. Suzuki, T.M. Pollock, and E. Spiecker: *Acta Mater.*, 2016, vol. 113, pp. 335–49.
26. L.P. Freund, O.M.D.M. Messé, J.S. Barnard, M. Göken, S. Neumeier, and C.M.F. Rae: *Acta Mater.*, 2017, vol. 123, pp. 295–304.
27. T.M. Smith, N.A. Zarkevich, A.J. Egan, J. Stuckner, T.P. Gabb, J.W. Lawson, and M.J. Mills: *Commun. Mater.*, 2021, vol. 2, p. 106.
28. T.M. Smith, B.D. Esser, N. Antolin, G.B. Viswanathan, T. Hanlon, A. Wessman, D. Mourer, W. Windl, D.W. McComb, and M.J. Mills: *Acta Mater.*, 2015, vol. 100, pp. 19–31.
29. L. Liliensten, S. Antonov, B. Gault, S. Tin, and P. Kontis: *Acta Mater.*, 2021, vol. 202, pp. 232–42.
30. S.K. Mäkinen, A. Kumar, M. Lenz, P. Kontis, T. Meiners, C. Zenk, S. Zaeferrer, G. Eggeler, S. Neumeier, E. Spiecker, D. Raabe, and B. Gault: *Acta Mater.*, 2018, vol. 155, pp. 362–71.
31. T.M. Smith, B.S. Good, T.P. Gabb, B.D. Esser, A.J. Egan, L.J. Evans, D.W. McComb, and M.J. Mills: *Acta Mater.*, 2019, vol. 172, pp. 55–65.
32. T.M. Smith, Y. Rao, Y. Wang, M. Ghazisaeidi, and M.J. Mills: *Acta Mater.*, 2017, vol. 141, pp. 261–72.
33. O.M. Messé, J.S. Barnard, E.J. Pickering, P.A. Midgley, and C.M.F. Rae: *Philos. Mag.*, 2014, vol. 94, pp. 1132–52.
34. H. Lukas, S.G. Fries, and B. Sundman: *Computational Thermodynamics: The Calphad Method*, 1st ed. Cambridge University Press, Cambridge, 2007.
35. J.-O. Andersson, T. Helander, L. Höglund, P. Shi, and B. Sundman: *Calphad*, 2002, vol. 26, pp. 273–312.
36. *Thermo-Calc Software, Database TCNI10, Version 2021b*, 2021.
37. S.Y. Yuan, Z.H. Jiang, J.Z. Liu, Y. Tang, and Y. Zhang: *Mater. Res. Lett.*, 2018, vol. 6, pp. 683–88.
38. A.J. Egan, Y. Rao, G.B. Viswanathan, T.M. Smith, M. Ghazisaeidi, S. Tin, and M.J. Mills: in *Superalloys 2020*, S. Tin, M. Hardy, J. Clews, J. Cormier, Q. Feng, J. Marcin, C. O'Brien, and A. Suzuki, eds., Springer, Cham, 2020, pp. 640–50.
39. D. Barba, T.M. Smith, J. Miao, M.J. Mills, and R.C. Reed: *Metall. Mater. Trans. A*, 2018, vol. 49A, pp. 4173–85.
40. L. Feng, S.B. Kannan, A. Egan, T. Smith, M.J. Mills, M. Ghazisaeidi, and Y. Wang: *Acta Mater.*, 2022, vol. 240, p. 118287.
41. F.D. León-Cázares, F. Monni, and C.M.F. Rae: *Acta Mater.*, 2020, vol. 199, pp. 209–24.
42. M. Lenz, Y.M. Eggeler, J. Müller, C.H. Zenk, N. Volz, P. Wollgramm, G. Eggeler, S. Neumeier, M. Göken, and E. Spiecker: *Acta Mater.*, 2019, vol. 166, pp. 597–610.
43. S. Lu, S. Antonov, L. Li, C. Liu, X. Zhang, Y. Zheng, H.L. Fraser, and Q. Feng: *Acta Mater.*, 2020, vol. 190, pp. 16–28.

44. A. Bezold, L. Amon, N. Karpstein, E. Spiecker, M. Göken, and S. Neumeier: *Scripta Mater.*, 2023, vol. 222, p. 115005.
45. Z. Zhang, Z. Yang, S. Lu, A. Harte, R. Morana, and M. Preuss: *Nat. Commun.*, 2020, vol. 11, p. 4890.
46. T.M. Smith, B.D. Esser, B. Good, M.S. Hooshmand, G.B. Viswanathan, C.M.F. Rae, M. Ghazisaeidi, D.W. McComb, and M.J. Mills: *Metall. Mater. Trans. A*, 2018, vol. 49A, pp. 4186–98.
47. X. Wu, S.K. Makineni, C.H. Liebscher, G. Dehm, J. RezaeiMianroodi, P. Shanthraj, B. Svendsen, D. Bürger, G. Eggeler, D. Raabe, and B. Gault: *Nat. Commun.*, 2020, vol. 11, p. 389.
48. S. Lu, S. Antonov, L. Li, and Q. Feng: *Metall. Mater. Trans. A*, 2018, vol. 49A, pp. 4079–89.

Publisher's Note Springer Nature remains neutral with regard to jurisdictional claims in published maps and institutional affiliations.